Robust optimal rendezvous using differential drag

Lamberto Dell'Elce*, Vladimir Martinusi†, and Gaëtan Kerschen‡
University of Liège, Liège, 4000, Belgium

The practical realization of the differential drag technique for orbital relative maneuvers must cope with the several and severe uncertainty sources affecting drag modeling. Neglecting these uncertainties might yield to oversimplified solutions whose representation of a real-life scenario is questionable. The first outcome of this study consists in the synthesis of a robust optimal controller which combines differential flatness theory and the scenario approach to generate a reference path which can be easily followed. The second outcome is the characterization of the relevant uncertainties of the differential drag problem, with a special focus on the aerodynamic force. The developments are validated in a highly detailed simulation environment including, among the perturbations, advanced drag modeling and coupled attitude and orbital dynamics.

I. Introduction

Differential drag is regarded as a promising technique in low-Earth orbits (LEO), since it allows to turn the often-undesired drag perturbation into a control force for relative maneuvers, e.g., formation keeping, rendez-vous, and cluster keeping.[1,2,3] This results into the reduction, or even the removal, of propellant needs for some missions and into consistent weight and volume saving. Nonetheless, relevant uncertainties in drag modeling make its practical realization a challenge, especially if no other propulsive means is available to accommodate them.

The main outcome of the paper is the development of a robust optimal control algorithm for differential drag maneuvers. The control loop consists of three main blocks analogous to the ones developed by the authors in.[4] The first block consists of a drag estimator and it is aimed at observing the two spacecraft and at deducing a fitted drag coefficient from their dynamics. In addition, this block is also in charge of the estimation of the uncertainties on the estimated drag. The second block is the maneuver planner. It is in charge of the computation of a robust optimal reference trajectory. The problem is solved by means of a direct transcription. Because the linearized dynamical system is differentially flat,[5] by exploiting the scenario approach,[6,7] we are able to get rid of the equality constraints (defects) of the optimization problem, to naturally include uncertainties in the constraints, and to quantitatively assess and impose a level of robustness of the solution. To put it another way, the scenario approach allows us to arbitrary define a percentage of the stochastic domain where the reference path is feasible.[8] Finally, the third block is aimed at coping with on-line compensation of the drift from the scheduled path. For this purpose, a model predictive control algorithm is exploited.

The second outcome of the paper is the characterization of the most relevant uncertainties of the differential drag problem, with a special focus on the aerodynamic force. The characterization is carried out by assuming operational conditions, i.e., it is based on the observation of the position of the satellites involved in the maneuver. In addition, historical dataset are used to build a probabilistic model of the space weather proxies. The resulting probabilistic model is exploited by the maneuver planner to generate a robust solution.

The paper is organized as follows: the rendez-vous problem analyzed and the notation are detailed in Section II. Section III summarizes few notions on differential flatness and on the scenario approach. The synthesis of the controller is discussed in Section IV. Finally, Section V provides with a numerical validation of the algorithm. The simulations are carried out in a highly detailed environment including advanced drag modeling and coupled attitude and orbital dynamics.

*PhD student, Aerospace and Mechanical Engineering Department, Chemin des Chevreuils 1, Liège, Belgium.
†Post-Doctoral Researcher, Aerospace and Mechanical Engineering Department, Chemin des Chevreuils 1, Liège, Belgium.
‡Professor, Aerospace and Mechanical Engineering Department, Chemin des Chevreuils 1, Liège, Belgium.

II. Rendez-vous using differential drag

This study is focused on the rendez-vous problem between two satellites, namely the target and the chaser, using differential drag as the only control force. It is assumed that the orbits of the satellites are near-circular and quasi coplanar. Though the former assumption could be eventually removed, it is not the case for the latter, which comes from the extremely modest authority of the differential drag in the out-of-plane direction. Specifically, Ben-Yaacov *et al.* showed that the controllability is two order of magnitude smaller in this direction even for highly inclined orbits.[11] For this reason, *the only in-plane position and velocity of the relative dynamics are controlled herein.*

The relative states are expressed in the mean local vertical local horizontal (LVLH) frame. The origin is in the target. The $\hat{\boldsymbol{x}}$ and the $\hat{\boldsymbol{z}}$ axes point toward the mean position vector[1] and the mean orbital momentum of the target, respectively. The $\hat{\boldsymbol{y}}$ axis completes the right-hand frame.

In the following of the paper, in-plane mean relative curvilinear coordinates, $\tilde{\boldsymbol{w}} = (\tilde{x}, \tilde{y}, \tilde{v}_x, \tilde{v}_y)^T$, are exploited instead of the Cartesian mean relative position and velocity, $\boldsymbol{w} = (x, y, \dot{x}, \dot{y})^T$:

$$\begin{aligned} \tilde{x} &= \sqrt{(r_t + x)^2 + y^2} - r_t & \tilde{v}_x &= \dot{x}\cos\alpha - \dot{y}\sin\alpha \\ \tilde{y} &= \sqrt{(r_t + x)^2 + y^2}\ \alpha & \tilde{v}_y &= \dot{x}\sin\alpha + \dot{y}\cos\alpha \end{aligned} \tag{1}$$

where r_t is the current mean radius of the target's orbit, and $\alpha = \tan^{-1}\frac{y}{r_t+x}$. The relative frame and the graphical interpretation of the curvilinear coordinates are illustrated in Figure 1.

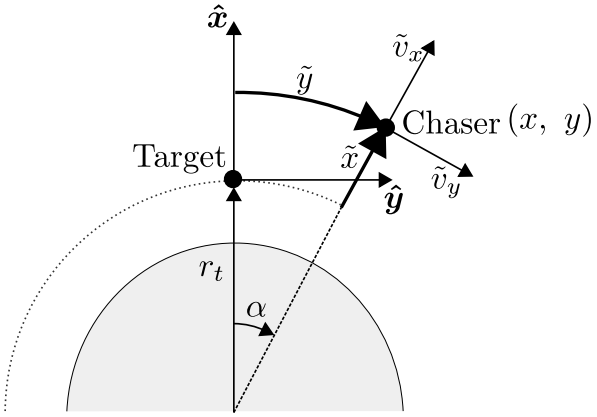

Figure 1. Relative frame and curvilinear states. The $\hat{\boldsymbol{z}}$ direction completes the right-hand frame.

The rendez-vous maneuver consist in the solution of the following two-point boundary value problem:

$$\begin{aligned} \frac{\mathrm{d}\tilde{\boldsymbol{w}}}{\mathrm{d}t} &= \nabla_{\boldsymbol{w}} \left\{ \begin{array}{c} \dot{x}\left(\tilde{\boldsymbol{w}}\right) \\ \dot{y}\left(\tilde{\boldsymbol{w}}\right) \\ \boldsymbol{f}\left(\tilde{\boldsymbol{w}}, t, \delta\right) \cdot \hat{\boldsymbol{x}} \\ \boldsymbol{f}\left(\tilde{\boldsymbol{w}}, t, \delta\right) \cdot \hat{\boldsymbol{y}} \end{array} \right\} + \left\{ \begin{array}{c} 0 \\ 0 \\ 0 \\ 1 \end{array} \right\} \Delta f_d\left(\tilde{\boldsymbol{w}}, t, \delta, u\right), \\ \tilde{\boldsymbol{w}}(0) &= \tilde{\boldsymbol{w}}_0, \\ \tilde{\boldsymbol{w}}\left(t_f\right) &= \boldsymbol{0}; \end{aligned} \tag{2}$$

here:

- $\tilde{\boldsymbol{w}}_0$ and t_f are the initial conditions and the maneuvering time, respectively;
- $\boldsymbol{f}\left(\tilde{\boldsymbol{w}}, t, \delta\right)$ consists of all the non-inertial accelerations and differential forces per unit mass but the differential drag contribution, which is expressed by the term Δf_d defined as:

$$\Delta f_d = \boldsymbol{f}_{d,c} \cdot \left(\sin\alpha\hat{\boldsymbol{x}} + \cos\alpha\hat{\boldsymbol{y}}\right) - \boldsymbol{f}_{d,t} \cdot \hat{\boldsymbol{y}} \tag{3}$$

[1] I.e., generated from the mean keplerian elements.

where $\boldsymbol{f}_{d,c}$ and $\boldsymbol{f}_{d,t}$ are the aerodynamic force per unit mass acting on the chaser and on the target, respectively. We note that no assumption is introduced on the direction of the aerodynamic force at this moment. Indeed, some assumptions are introduced in the synthesis of the controller (see Section IV), but not in the numerical simulations (see Section V). All the remaining components of the differential aerodynamic force vector, i.e., $\boldsymbol{f}_{d,c} - \boldsymbol{f}_{d,t}$, are included in $\boldsymbol{f}\left(\tilde{\boldsymbol{w}}, t, \delta\right)$.

- δ represents the uncertain environment. Indeed, δ includes all the stochastic uncertainties affecting the aerodynamic force and the other orbital perturbations, e.g., solar radiation pressure and non-modeled gravitational harmonics, but it is not necessary limited to them. To put it another way, δ represents anything affecting the dynamic evolution of the states which is not modeled by means of a deterministic contribution in $\boldsymbol{f}$, i.e., depending *only* on $\tilde{\boldsymbol{w}}$ and t. For instance, because the out-of plane relative position is not among state variables, its influence on the evolution of $\tilde{\boldsymbol{w}}$ is part of the uncertain set.

- u is the control variable. Differential drag is imposed by controlling the relative ballistic coefficient between the chaser and the target. This can be achieved either by means of the reorientation of solar panels or through attitude control. Because the aerodynamic force is uncertain, it is not possible to directly impose a desired value of differential drag. So, regardless the method, we define the control variable, $u(t) \in [-1, 1]$ such that:

$$\Delta f_d(\tilde{x}, t, \delta, 1) = \max_u \left(\Delta f_d(\tilde{x}, t, \delta, u)\right), \quad \Delta f_d(\tilde{x}, t, \delta, -1) = \min_u \left(\Delta f_d(\tilde{x}, t, \delta, u)\right). \tag{4}$$

  Because in the numerical simulations we do not make the assumption that the aerodynamic force is proportional to cross section and that there is not lift, the configurations of the spacecraft corresponding to $u = 1$ and $u = -1$ are not deterministically defined. However, a very good approximation consists in choosing $u = 1$ such that the chaser and the target have their minimum and maximum cross section exposed to their own orbital velocity, respectively, and *vice versa* for $u = -1$.

The main challenge associated to the practical exploitation of differential drag is that the huge uncertainty in the magnitude of the control force.

III. Mathematical background

3.A. Differential flatness

Differential flatness was first introduced by Fliess.[9] The use of differential flatness for the planning of orbital rendez-vous maneuvers was proposed by Louembet.[10] Consider a dynamical system $\dot{\boldsymbol{w}} = \boldsymbol{f}\left(\boldsymbol{w}, \boldsymbol{u}\right)$ with n states, $\boldsymbol{w}(t) : \mathbb{R} \to \mathbb{R}^n$, and $m \leq n$ inputs, $\boldsymbol{u}(t) : \mathbb{R} \to \mathbb{R}^m$. The system is said flat if a set of m variables

$$\boldsymbol{q} = \boldsymbol{\mathcal{Q}}\left(\boldsymbol{w}, \boldsymbol{u}, \dot{\boldsymbol{u}}, \ddot{\boldsymbol{u}}, \ldots\right), \tag{5}$$

exists such that

$$\begin{aligned} \boldsymbol{w} &= \boldsymbol{\mathcal{W}}\left(\boldsymbol{q}, \dot{\boldsymbol{q}}, \ddot{\boldsymbol{q}}, \ldots\right), \\ \boldsymbol{u} &= \boldsymbol{\mathcal{U}}\left(\boldsymbol{q}, \dot{\boldsymbol{q}}, \ddot{\boldsymbol{q}}, \ldots\right). \end{aligned} \tag{6}$$

The variables $\boldsymbol{q} \in \mathbb{R}^m$ are referred to as *flat outputs*.

Flatness is a property of the system. Proving that a system is flat is not necessary an easy task. Linear systems are differentially flat if and only if they are controllable.

The important property of the flatness exploited in this paper is that given a sufficiently smooth trajectory for the flat outputs, $\boldsymbol{q}(t)$, the corresponding time evolution of the states and the control necessary to obtain the trajectory are analytically determined by mapping $\boldsymbol{q}(t)$ through $\boldsymbol{\mathcal{W}}$ and $\boldsymbol{\mathcal{U}}$, respectively.

3.B. The scenario approach

Consider the robust optimization problem

$$\begin{aligned} \boldsymbol{y}^* = \arg \left[\min_{\boldsymbol{y}} \left(\boldsymbol{c}^T \boldsymbol{y}\right)\right] \qquad & s.t.: \\ \boldsymbol{g}(\boldsymbol{y}, \delta) \leq \boldsymbol{0} \qquad & \forall \delta \in \Delta. \end{aligned} \tag{7}$$

where $\boldsymbol{y} \in \mathbb{R}^d$, $\delta \in \Delta$, $\boldsymbol{c}$, and $\boldsymbol{g}$ are the d-dimensional vector of design variables, a generic random quantity (e.g., a set of random variables and stochastic processes) defined on the sample space Δ and provided with probability distribution P_Δ, a constant vector, and a set of constraints, respectively. The optimal solution of Problem 7 is robust all over the uncertain domain Δ. In other words, given any sample $\delta \in \Delta$, $\boldsymbol{y}^*$ is feasible, i.e., $\boldsymbol{g}(\boldsymbol{y}^*, \delta) \leq \mathbf{0}$.

When the event space of Δ is infinite-dimensional – as it is most often the case – solving Problem 7 can be a real challenge. In this case, because the number of design variables is finite, the problem is called *semi-infinite*. The scenario approach is a tool that allows to solve a relaxed version of the *semi-infinite* Problem 7, where the obtained solution is only feasible in a subset $\Delta_\epsilon \in \Delta$ such that $P_\Delta(\Delta_\epsilon) \geq 1 - \epsilon$. Here $\epsilon \in (0, 1]$ is referred to as *risk parameter*.

Consider problem 7 and assume that $\boldsymbol{g}$ is convex with respect to $\boldsymbol{y}$. The scenario approach states that:

> given a *confidence parameter* $\beta \in [0, 1)$, a risk ϵ, and s *independent* instances $(\delta_1, \ldots, \delta_s)$ of Δ extracted according to P_Δ and such that
>
> $$s \geq \frac{2}{\epsilon}\left(d - \ln \beta\right), \tag{8}$$
>
> the solution of the *finite*-dimensional problem
>
> $$\begin{aligned} \boldsymbol{y}^* = \arg \left[\min_{\boldsymbol{y}} \left(\boldsymbol{c}^T \boldsymbol{y}\right)\right] \qquad & s.t.: \\ \boldsymbol{g}(\boldsymbol{y}, \delta_1) &\leq \mathbf{0} \\ &\vdots \\ \boldsymbol{g}(\boldsymbol{y}, \delta_s) &\leq \mathbf{0} \end{aligned} \tag{9}$$
>
> satisfies all the constraints in Δ but at most a portion ϵ with probability $1 - \beta$.

One of the most appealing features of the scenario approach, is that the risk ϵ is selected by the user, so that it can be made as small as desired. Furthermore, since the only requirement for the scenario approach is the *convexity* with respect to design variables, it has an extremely high level of generality and no requirement exists for the uncertain set.

We note that the confidence parameter, β, appears as the argument of a logarithm in Equation (8). When β approaches 0 its logarithm decreases slowly. For practical purposes, the confidence parameter can be chosen small enough to be neglected for any practical purpose, e.g., $\beta = 10^{-7} \Rightarrow -\ln \beta \simeq 16$.

Another very interesting property of the scenario approach is that *it does not require a probabilistic characterization of the stochastic sources* of the problem. In fact, even though it assumes the existence of a probability distribution P_Δ, it does not require its knowledge, but it only requires the realization of a certain number of samples. For this reason, the scenario approach facilitates the inclusion of uncertainty sources of arbitrary nature in the dynamics, e.g., random variables, stochastic processes, and random fields. Assume, for example, that the uncertainty due to the high order harmonics of the gravitational field are included in the rendez-vous problem. Because the variance of this perturbation decreases with the relative distance and because it also depends on time given a fixed relative position, this uncertainty should be properly characterized by means of a non-uniform and non-stationary random field dependent on the relative position and on time. However, with the scenario approach it is only sufficient to generate a certain number of samples. This can be achieved, for example, by comparing the specific force of the reference dynamics equations with respect to a higher precision propagation.

More advanced and detailed results on the scenario approach are available in the references.[6,7,8]

IV. Control algorithm

The proposed optimal control strategy consists of three modules: 1) the probabilistic drag estimator evaluates the ballistic coefficient of the two satellites in their minimum and maximum differential drag configuration and it computes a probabilistic model for the drag, 2) the maneuver planner schedules an optimal reference trajectory, 3) The on-line compensator corrects the deviations from the reference path due to non-modeled dynamics and uncertainties. The high-level control strategy is illustrated in Fig. 2.

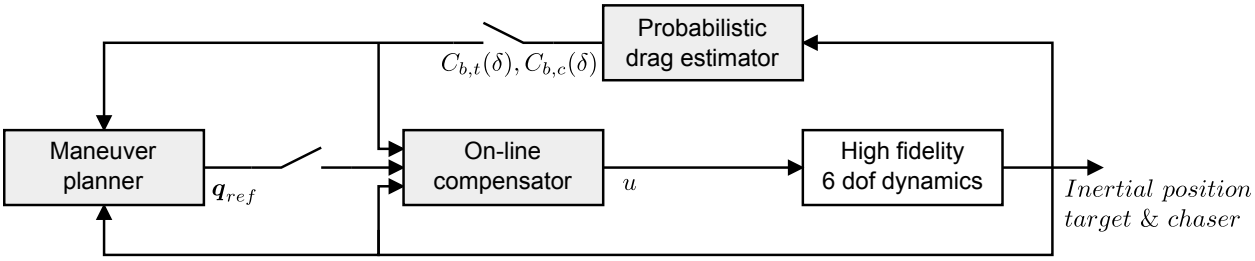

Figure 2. High-level optimal control strategy.

The drag estimator and the maneuver planner are activated few times within the maneuver. We note that the maneuver planner requires computational resources which might not be available on board, especially when considering small satellites. However, because this task is executed sporadically, the computation of the reference path can be performed on-ground and uploaded. In this work, we only execute both the drag estimator and the maneuver planner once at the beginning.

4.A. Probabilistic drag estimator

The probabilistic drag estimator is in charge of delivering to the maneuver planner: 1) a deterministic "best fit" of the differential drag force, 2) a probabilistic model for its uncertainties. For this purpose, it requires that the accurate position position of the target and the chaser is monitored for an observation time t_{obs}. The configuration of the satellites (i.e., attitude or orientation of the drag panels) is imposed throughout this period such that:

$$u(t) = \begin{cases} +1 & \forall\ 0 \leq t \leq \frac{t_{obs}}{2} \\ -1 & \forall\ \frac{t_{obs}}{2} < t \leq t_{obs} \end{cases} \tag{10}$$

1. Deterministic component

The deterministic fit relies on some simplifying assumptions, namely: the drag is assumed to be the only component of the aerodynamic force, the force is proportional to the local atmospheric density, ρ, and the ballistic coefficient of the target and of the chaser, $C_{b,t}$ and $C_{b,c}$, is constant and varies linearly with u[1].

The deterministic ballistic coefficients are estimated by minimizing the drift between observed and simulated relative position. Simulated data can be generated on-board through a low-precision propagation including J_2 gravitational effect and drag perturbation only. The aerodynamic force of the simulated data is given by:

$$\boldsymbol{f}_d^{(det)} = -\frac{1}{2}\rho C_b(u)\,||\boldsymbol{v}_{TAS}||\,\boldsymbol{v}_{TAS} \tag{11}$$

where $\boldsymbol{v}_{TAS} = \boldsymbol{v} - \boldsymbol{\Omega}_e \times \boldsymbol{r}$, C_b, ρ, $\boldsymbol{r}$, $\boldsymbol{v}$, and $\boldsymbol{\Omega}_e$ are the airspeed, the ballistic coefficient, the atmospheric density, the inertial position and velocity, and the angular velocity of the Earth, respectively. A basic analytical model is exploited to estimate the density:

$$\rho\,(r, \theta, i; A, B, C, D) = A\,(1 + B\cos\,(\theta - C))\exp\left(\frac{r - r_e\sqrt{1 - e_e^2\sin^2 i\sin^2\theta}}{D}\right) \tag{12}$$

where θ, i, (A, B, C, D), r_e, and e_e, are the mean argument of latitude and orbital inclination, the calibration coefficients of the model, and the equatorial radius and the eccentricity of the Earth, respectively. Though relatively simple, this model is able to outline the more relevant characteristics of the upper atmosphere, namely the exponential vertical structure, the day-night bulge, and the oblateness of the Earth. The coefficients of the model are orbit-dependent and they were tuned using the Jacchia 71 model. We note that

[1]Under these assumptions, the exposed cross sections to the incoming flow of the target and of the chaser are linearly dependent on the control variable u.

the calibration of the simple model is not performed with the same model exploited for the high fidelity simulations presented in Section V, i.e., NRLMSISE-00. This is motivated by the scope of the paper to consider a realistic scenario. In this way, the controller does not know the exact structure of the atmosphere.

The estimation is performed by solving:

$$\begin{aligned} C_{b,t}(u) =& \arg\left[\min_{C_b}\left(\int_{\frac{t_{obs}}{2}\frac{u-1}{2}}^{\frac{t_{obs}}{2}\frac{u+1}{2}} \left(\boldsymbol{r}_{obs,t}-\boldsymbol{r}_{sim,t}\left(C_b\right)\right)^2 \mathrm{d}t\right)\right], \\ C_{b,c}(u) =& \arg\left[\min_{C_b}\left(\int_{\frac{t_{obs}}{2}\frac{u-1}{2}}^{\frac{t_{obs}}{2}\frac{u+1}{2}} \left(\boldsymbol{r}_{obs,c}-\boldsymbol{r}_{sim,c}\left(C_b\right)\right)^2 \mathrm{d}t\right)\right] \end{aligned}, \qquad u=\pm 1 \tag{13}$$

Here, $\boldsymbol{r}_{obs}$ and $\boldsymbol{r}_{sim}$ are the observed and simulated inertial position, respectively. The subscripts t and c indicate the target and the chaser, respectively.

The necessary condition for the exploitation of the differential drag is that the estimated differential ballistic coefficient, $\Delta C_b(u) = C_{b,c}(u) - C_{b,t}(u)$, is such that $\Delta C_b(1) < 0$ and $\Delta C_b(-1) > 0$. In this case, the target is said to be feasible.

Finally, the deterministic component of the differential drag is given by:

$$\Delta f_d^{(det)}\left(t,\boldsymbol{w},u\right) = \boldsymbol{f}_{d,c}^{(det)}\left(t,u,\boldsymbol{r}_{sim,t}(t)+\boldsymbol{w}\right)\cdot\left(\sin\alpha\hat{\boldsymbol{x}}+\cos\alpha\hat{\boldsymbol{y}}\right) - \boldsymbol{f}_{d,t}^{(det)}\left(t,u,\boldsymbol{r}_{sim,t}(t)\right)\cdot\hat{\boldsymbol{y}} \tag{14}$$

where the dependency on the inertial states is disappeared because they are replaced by the low fidelity simulation of the position of the target, $\boldsymbol{r}_{sim,t}(t)$.

2. *Stochastic component*

The probabilistic model provided by the drag estimator is defined as follows:

$$\Delta f_d = \gamma(t,\delta)\Delta f_d^{(det)}\ \left(t,\boldsymbol{w},u\right) \tag{15}$$

where $\{\gamma(t,\delta),\ t\in\mathbb{R}^+\}$ is a non-stationary stochastic process defined on a probability triple $(\Delta,\mathcal{F}_\Delta,P_\Delta)$ indexed by $\mathbb{R}^+$ with values in $\mathbb{R}^+$.

The process $\gamma(t,\delta)$ is decomposed into a fast and a slow contributions, $\gamma_{fast}\left(t,\delta\right)$ and $\gamma_{slow}\left(t,\delta\right)$, respectively, such that $\gamma(t,\delta) = \gamma_{fast}(t,\delta)\ \gamma_{slow}(t,\delta)$. The fast component accounts for variations with time scale smaller than the orbital period, while the slow components is introduced to account for longer-term variations of the atmospheric density, i.e., of the order of one or more days. They are characterized in the following.

Fast variations are modeled by means of a seasonal auto-regressive moving average process (SARMA), $ARMA(n_{ar},n_{ma})_{n_s}$, where n_{ar}, n_{ma}, and n_s are the order of the auto-regressive and moving average polynomials, and the seasonal order, respectively.

Given the sequence of observations of the relative states during the observation time,

$$\left\{\tilde{\boldsymbol{w}}_{obs}\left(t_i\right),\ t_i=\frac{i}{n_{obs}}t_{obs},\ i=0,\ldots,n_{obs}\right\},$$

the seasonal order is chosen such that the period of the seasonal component is approximatively the orbital one, i.e., $n_s = \text{round}\left(\frac{t_{orb}}{t_{obs}}n_{obs}\right)$. The estimation of the coefficients of the SARMA process is then carried out by using the sequence of data:

$$\left\{\frac{\mathrm{D}_1\left(\tilde{v}_{y,obs}\left(t_i\right)\right)+2\omega_{orb}c\ \tilde{v}_{x,obs}\left(t_i\right)}{\Delta f_d^{(det)}\left(t_i,\tilde{\boldsymbol{w}}_{obs}\left(t_i\right),u(t_i)\right)},\ i=0,\ldots,n_{obs}\right\} \tag{16}$$

where $\omega_{orb}=\frac{2\pi}{t_{orb}}$ and $c=\sqrt{1+\frac{3}{8}\frac{J_2\ R_e^2}{a^2}\left(1+3\cos 2i\right)}$, i_{orb}, and R_e are the constant angular orbital velocity, the Scweighart-Sedwick coefficient, the orbital inclination, and the Earth's equatorial radius, respectively. The operator $\mathrm{D}_1\left(\cdot\right)$ indicates a numerical approximation of the time derivative, e.g., by means of centered finite differences.

The exploitation of the sequence of Equation (16) for the characterization of γ_{short} is due to the use of the Schweighart-Sedwick equations[12] in the controller plant, as detailed in Section 4.B.

We note that the uncertainty in γ_{fast} cannot be attributed to the only uncertainties in the drag estimation, but it also includes all the non-modeled perturbations, e.g., high order harmonics of the gravity field or perturbations of the apparent forces, navigation errors, model error of the Schweighart-Sedwick equations, and errors introduced by the differentiation using D_1 as well.

Slow variations arise from more relevant changes of the magnitude of the atmospheric density. These are mainly due to the correlation between the atmospheric density itself and the solar and geomagnetic activities, which are stochastic processes in nature. Daily and 81-day averaged solar activity, $F_{10.7}$ and $\bar{F}_10.7$ and daily geomagnetic index, A_P, are widely exploited proxies exploited in upper atmosphere models, e.g., Jacchia 71 and NRLMSISE-00. A probabilistic characterization of these proxies was proposed by the authors in[13] and[14] and it is summarized in the following.

The characterization of the proxies is carried out by using the data measured over the last 50 years provided by the Celestrack database.[15] A reduced set of data is retained according to the mission window, i.e., the only data of the previous cycles that correspond to the same portion of the solar cycle are exploited for uncertainty characterization.

Given the maximum duration of the maneuver, t_f, the duration of the stochastic process, t_{proc}, must be no smaller than this. The three stochastic processes are modeled as three arrays of correlated random variables. Given the short time span of the maneuvers compared to the solar cycle, the processes are reasonably assumed to be stationary within the maneuvering time, i.e., the random variables used for the modeling of the sequence of each of the three proxies are assumed to have the same marginal distribution. For this purpose, the selected dataset is split into sequences of length $n_{kn} = \mathrm{ceil}(\frac{t_{proc}}{86400\ \mathrm{s}})$. The three correlated stochastic processes are modeled by means of three n_{kn}-elements vectors of random variables, $\mathbf{F}_{10.7}$, $\bar{\mathbf{F}}_{10.7}$, and $\mathbf{A}_p$, such that the generic k-th element is the value of the proxy evaluated at time $t_k = k$ 86400 s.

The following Gaussian copula is used to account for the statistical dependence both within and among $\mathbf{F}_{10.7}$, $\bar{\mathbf{F}}_{10.7}$, and $\mathbf{A}_p$:

$$\left.\begin{matrix}\boldsymbol{Z}_1\\ \boldsymbol{Z}_2\\ \boldsymbol{Z}_3\end{matrix}\right\} \xrightarrow{\mathrm{chol}(\mathcal{C})} \left\{\begin{matrix}\boldsymbol{\Xi}_1 & \xrightarrow{c_N(\boldsymbol{\xi}_1)} & \boldsymbol{U}_1 & \xrightarrow{\mathcal{F}^{-1}_{F_{10.7}}\left(\boldsymbol{u}_1;\boldsymbol{\vartheta}_{F_{10.7}}\right)} & \mathbf{F}_{10.7}\\ \boldsymbol{\Xi}_2 & \xrightarrow{c_N(\boldsymbol{\xi}_2)} & \boldsymbol{U}_2 & \xrightarrow{\mathcal{F}^{-1}_{\bar{F}_{10.7}}\left(\boldsymbol{u}_2;\boldsymbol{\vartheta}_{\bar{F}_{10.7}}\right)} & \bar{\mathbf{F}}_{10.7}\\ \boldsymbol{\Xi}_3 & \xrightarrow{c_N(\boldsymbol{\xi}_3)} & \boldsymbol{U}_3 & \xrightarrow{\mathcal{F}^{-1}_{A_p}\left(\boldsymbol{u}_3;\boldsymbol{\vartheta}_{A_p}\right)} & \mathbf{A}_p\end{matrix}\right. ; \tag{17}$$

here

- $\boldsymbol{Z}_1$, $\boldsymbol{Z}_2$, and $\boldsymbol{Z}_3$ are n_{kn}-element vectors of independent standard Gaussian random variables,
- $\boldsymbol{\Xi}_1$, $\boldsymbol{\Xi}_2$, and $\boldsymbol{\Xi}_3$ are n_{kn}-element vectors of correlated standard Gaussian random variables; $\mathrm{chol}\,(\mathcal{C})$ is the Cholesky decomposition of their correlation matrix. It holds $\left[\boldsymbol{\Xi}_1^T, \boldsymbol{\Xi}_2^T, \boldsymbol{\Xi}_3^T\right] = \left[\boldsymbol{Z}_1^T, \boldsymbol{Z}_2^T, \boldsymbol{Z}_3^T\right] \mathrm{chol}\,(C)$,
- $\boldsymbol{U}_1$, $\boldsymbol{U}_2$, and $\boldsymbol{U}_3$ are n_{kn}-element vectors of correlated uniform random variables with support [0, 1],
- $\mathcal{F}_{(\cdot)}$ is the cumulative distribution function (CDF) of the marginal distribution that is chosen to fit the model, and $\boldsymbol{\vartheta}_{(\cdot)}$ is the vector of parameters defining the distribution.

Histogram are exploited to model the marginal probability density distributions. The value of the proxies is then interpolated to yield a continuous process in time.

After characterizing the proxies with the cupola process, their uncertainty is recast into γ_{slow} as follows:

$$\gamma_{slow}(t,\delta) = \frac{\rho_{J_{71}}\left(\boldsymbol{r}_{sim,t}(t), t; F_{10.7}(t,\delta), \bar{F}_{10.7}(t,\delta), A_p(t,\delta)\right)}{\rho\left(r_{sim,t}(t), \theta_{sim,t}(t), i_{sim_t}(t); A, B, C, D\right)} \tag{18}$$

where $\rho_{J_{71}}$ is the atmospheric density computed with the Jacchia 71 model.

4.B. Maneuver planner

The maneuver planner schedules a robust optimal reference trajectory for the rendez-vous maneuver. The methodology for robust maneuver planning of differentially flat system proposed by the authors in[5] is exploited for this purpose. This methodology is detailed in the following, and it is then applied to the differential drag problem in analysis.

1. Mathematical formulation of the robust maneuver planning

Consider the robust optimal control formulation of a generic two-point boundary value problem:

$$\begin{aligned} \boldsymbol{w}^* = \arg \left[\min_{\boldsymbol{w}(t),\ t\in[0,T]} \left(\max_{\delta\in\Delta} \mathcal{J}(\boldsymbol{w},\delta) \right) \right] \qquad & s.t.: \\ \dot{\boldsymbol{w}} = \ \boldsymbol{f}\left(\boldsymbol{w},\boldsymbol{u},\delta\right) \qquad & \forall\ t\in[0,T]\ \wedge\ \delta\in\Delta \\ \boldsymbol{g}\left(\boldsymbol{w},\boldsymbol{u},\delta\right) \leq \boldsymbol{0} \qquad & \forall\ t\in[0,T]\ \wedge\ \delta\in\Delta \\ \boldsymbol{w}(0) = \boldsymbol{w}_0 & \\ \boldsymbol{w}(T) = \boldsymbol{0}, & \end{aligned} \tag{19}$$

where $\mathcal{J}:\mathbb{R}^n\times\Delta\to\mathbb{R}$, $\boldsymbol{f}\in\mathbb{R}^n$, $\boldsymbol{w}\in\mathbb{R}^n$, $\boldsymbol{u}\in\mathbb{R}^m$, $\delta\in\Delta$, T, and $\boldsymbol{w}_0$ are the objective function (convex with respect to $\boldsymbol{w}$), the right hand terms of the stochastic dynamics equations, the dynamic states, the control forces per unit mass, a generic uncertain quantity defined on Δ, the maneuvering time, i.e., the time when rendez-vous conditions are met, and the initial state vector, respectively. $\boldsymbol{g}\in\mathbb{R}^c$ expresses constraints like the saturation of the control variables.

The objective of Problem 19 is to find a *deterministic trajectory* of the states which is robust against uncertainties in the dynamics, i.e., which could be ideally followed for any instance of the uncertain environment $\delta\in\Delta$.

This problem is *infinite*-dimensional because the design variables are continuous in time, and the feasibility must be imposed on both the time range and the uncertain set. *The proposed methodology combines differential flatness and scenario approach to achieve a discretization of the time and the uncertain domain, respectively.*

Assume that a set of m flat outputs, $\boldsymbol{q}=\boldsymbol{\mathcal{Q}}\left(\boldsymbol{w},\boldsymbol{u},\dot{\boldsymbol{u}},\ddot{\boldsymbol{u}},\ldots\right)$, is available such that

$$\begin{aligned} \boldsymbol{w} \ &= \boldsymbol{\mathcal{W}}\left(\boldsymbol{q},\dot{\boldsymbol{q}},\ddot{\boldsymbol{q}},\ldots\right), \\ \boldsymbol{u} \ &= \boldsymbol{\mathcal{U}}\left(\boldsymbol{q},\dot{\boldsymbol{q}},\ddot{\boldsymbol{q}},\ldots,\delta\right). \end{aligned} \tag{20}$$

We note that the only mapping $\boldsymbol{\mathcal{U}}$ is allowed to be non-deterministic, i.e., dependent on δ. Problem 19 is then recast into

$$\begin{aligned} \boldsymbol{q}^* = \arg \left[\min_{\boldsymbol{q}(t),\ t\in[0,T]} \left(\max_{\delta\in\Delta} \tilde{\mathcal{J}}(\boldsymbol{q},\delta) \right) \right] \qquad & s.t.: \\ \tilde{\boldsymbol{g}}\left(\boldsymbol{q},\delta\right) \leq \boldsymbol{0} \qquad & \forall\ t\in[0,T]\ \wedge\ \delta\in\Delta \\ \boldsymbol{\mathcal{W}}\left(\boldsymbol{q}(0),\dot{\boldsymbol{q}}(0),\ddot{\boldsymbol{q}}(0),\ldots\right) = \boldsymbol{w}_0 & \\ \boldsymbol{\mathcal{W}}\left(\boldsymbol{q}(T),\dot{\boldsymbol{q}}(T),\ddot{\boldsymbol{q}}(T),\ldots\right) = \boldsymbol{0} & \end{aligned} \tag{21}$$

where $\tilde{\mathcal{J}}(\boldsymbol{q},\delta)=\mathcal{J}(\boldsymbol{\mathcal{W}}(\boldsymbol{q},\dot{\boldsymbol{q}},\ddot{\boldsymbol{q}},\ldots),\delta)$ and $\tilde{\boldsymbol{g}}(\boldsymbol{q},\delta)=\boldsymbol{g}(\boldsymbol{\mathcal{W}}(\boldsymbol{q},\dot{\boldsymbol{q}},\ddot{\boldsymbol{q}},\ldots),\boldsymbol{\mathcal{U}}(\boldsymbol{q},\dot{\boldsymbol{q}},\ddot{\boldsymbol{q}},\ldots,\delta),\delta)$. This formulation is still infinite-dimensional, but, thanks to differential flatness, the dynamics equations $\dot{\boldsymbol{w}}=\ \boldsymbol{f}\left(\boldsymbol{w},\boldsymbol{u},\delta\right)$ are automatically satisfied and they do not need to be enforced as equality constraints any more, e.g., by means of a pseudospectral transcription.

The discretization in time is performed by expressing the flat outputs in function of a basis of l sufficiently regular shape functions, $\boldsymbol{\Phi}(t)=[\phi_1(t),\ldots,\phi_l(t)]^T$:

$$\boldsymbol{q}^{(i)} = \sum_{j=1}^{l} \phi_j^{(i)}(t)\boldsymbol{q}_j = \boldsymbol{Q}\boldsymbol{\Phi}^{(i)}(t) \tag{22}$$

where the superscripts (i) are the order of the time derivative, and $\boldsymbol{Q}\in\mathbb{R}^{m\times l}$ is a matrix of coefficients with columns $\boldsymbol{q}_j$. The minimum regularity of the shape functions is determined by the maximum order of the derivative of $\boldsymbol{q}(t)$ in the mapping of Equation (20).

To remove the boundary conditions in Problem (21), the basis $\boldsymbol{\Phi}$ is projected into its subspace which satisfies them. For this purpose, $\boldsymbol{\Phi}$ is partitioned into $l-2n$ independent and $2n$ dependent elements[1] $\boldsymbol{\Phi}=\begin{bmatrix}\boldsymbol{\Phi}_{ind}\\ \boldsymbol{\Phi}_{dep}\end{bmatrix}$. An analogous partition is performed for the corresponding columns of $\boldsymbol{Q}$, which is rearranged

[1] the choice of dependent functions is arbitrary provided that $\left[\boldsymbol{\Phi}_{dep}(0),\dot{\boldsymbol{\Phi}}_{dep}(0),\ldots,\boldsymbol{\Phi}_{dep}(T),\dot{\boldsymbol{\Phi}}_{dep}(T),\ldots\right]$ is not singular.

as $\boldsymbol{Q} = \left[\boldsymbol{Q}_{ind}, \boldsymbol{Q}_{dep}\right]$. The discretized flat output becomes

$$\boldsymbol{q}^{(i)} = \boldsymbol{Q}_{ind}\tilde{\boldsymbol{\Phi}}^{(i)}(t) + \boldsymbol{\Psi}^{(i)}(t) \tag{23}$$

where

$$\begin{aligned}
\tilde{\boldsymbol{\Phi}}^{(i)}(t) &= \boldsymbol{\Phi}^{(i)}_{ind}(t) - \left[\boldsymbol{\Phi}_{ind}(0), \dot{\boldsymbol{\Phi}}_{ind}(0), \ldots, \boldsymbol{\Phi}_{ind}(T), \dot{\boldsymbol{\Phi}}_{ind}(T), \ldots\right] \\
&\qquad \left[\boldsymbol{\Phi}_{dep}(0), \dot{\boldsymbol{\Phi}}_{dep}(0), \ldots, \boldsymbol{\Phi}_{dep}(T), \dot{\boldsymbol{\Phi}}_{dep}(T), \ldots\right]^{-1} \boldsymbol{\Phi}^{(i)}_{dep}(t), \\
\boldsymbol{\Psi}^{(i)}(t) &= \left[\boldsymbol{q}(0), \dot{\boldsymbol{q}}(0), \ldots, \boldsymbol{q}(T), \dot{\boldsymbol{q}}(T), \ldots\right] \\
&\qquad \left[\boldsymbol{\Phi}_{dep}(0), \dot{\boldsymbol{\Phi}}_{dep}(0), \ldots, \boldsymbol{\Phi}_{dep}(T), \dot{\boldsymbol{\Phi}}_{dep}(T), \ldots\right]^{-1} \boldsymbol{\Phi}^{(i)}_{dep}(t),
\end{aligned}$$

and $\boldsymbol{q}(0), \dot{\boldsymbol{q}}(0), \ldots$ and $\boldsymbol{q}(T), \dot{\boldsymbol{q}}(T), \ldots$ are the boundary conditions of $\boldsymbol{q}$, and they are solution of $\boldsymbol{\mathcal{W}}\left(\boldsymbol{q}(0), \dot{\boldsymbol{q}}(0), \ldots\right) = \boldsymbol{w}_0$ and $\boldsymbol{\mathcal{W}}\left(\boldsymbol{q}(T), \dot{\boldsymbol{q}}(T), \ldots\right) = \boldsymbol{0}$, respectively. This is possible because the relationship between states and flat outputs is assumed to be deterministic, and so are the boundary conditions of $\boldsymbol{q}(t)$.

The time discretization is finalized by limiting the satisfaction of the constraints $\tilde{\boldsymbol{g}}$ to a discrete number p of check points, $t_1, \ldots, t_p$. The number and location of the check points can be either deduced from the properties of the basis, or it can be assessed by picking a number of uniformly-distributed random check points in $[0, T]$ according to Equation (8). In this latter case, the risk ϵ should be extremely small. The first option is pursued in this paper.

At this point, Problem (21) is reduced to the *semi-infinite approximation*

$$\begin{aligned}
\boldsymbol{Q}^*_{ind} = \arg \Bigg[\min_{\boldsymbol{Q}_{ind} \in \mathbb{R}^{m \times (l-2n)}} \left(\max_{\delta \in \Delta} \tilde{\mathcal{J}}(\boldsymbol{Q}_{ind}\tilde{\boldsymbol{\Phi}}(t) + \boldsymbol{\Psi}(t), \delta) \right) \Bigg] \qquad & s.t.: \\
\tilde{\boldsymbol{g}}\left(\boldsymbol{Q}_{ind}\tilde{\boldsymbol{\Phi}}(t_k) + \boldsymbol{\Psi}(t_k), \delta\right) \leq \boldsymbol{0} \qquad & k = 1, \ldots, p;\ \forall \delta \in \Delta
\end{aligned} \tag{24}$$

The scenario approach can now be exploited to solve Problem 24. For this purpose, we note that the objective function can be written under the form of Problem 7 by introducing a slack design variable, h, such that

$$\begin{aligned}
[\boldsymbol{Q}^*_{ind}, h^*] = \arg \left[\min_{\boldsymbol{Q}_{ind} \in \mathbb{R}^{m \times (l-2n)}, h \in \mathbb{R}} h \right] \qquad & s.t.: \\
\tilde{\mathcal{J}}(\boldsymbol{Q}_{ind}\tilde{\boldsymbol{\Phi}}(t) + \boldsymbol{\Psi}(t), \delta) - h \leq 0 \qquad & \forall \delta \in \Delta \\
\tilde{\boldsymbol{g}}\left(\boldsymbol{Q}_{ind}\tilde{\boldsymbol{\Phi}}(t_k) + \boldsymbol{\Psi}(t_k), \delta\right) \leq \boldsymbol{0} \qquad & k = 1, \ldots, p;\ \forall \delta \in \Delta
\end{aligned} \tag{25}$$

So, given an acceptable risk ϵ, and a confidence parameter β (small enough to be considered zero for practical purposes), and s independent samples $(\delta_1, \ldots, \delta_s) \in \Delta$ such that Equation (8) is satisfied (here $d = (l-2n)m + 1$), Problem 24 is recast in the discrete form

$$\begin{aligned}
\boldsymbol{Q}^*_{ind} = \arg \Bigg[\min_{\boldsymbol{Q}_{ind} \in \mathbb{R}^{m \times (l-2n)}} \left(\max_{\delta \in (\delta_1, \ldots, \delta_s)} \tilde{\mathcal{J}}(\boldsymbol{Q}_{ind}\tilde{\boldsymbol{\Phi}}(t) + \boldsymbol{\Psi}(t), \delta) \right) \Bigg] \qquad & s.t.: \\
\tilde{\boldsymbol{g}}\left(\boldsymbol{Q}_{ind}\tilde{\boldsymbol{\Phi}}(t_k) + \boldsymbol{\Psi}(t_k), \delta_1\right) \leq \boldsymbol{0} \qquad & k = 1, \ldots, p \\
\vdots & \\
\tilde{\boldsymbol{g}}\left(\boldsymbol{Q}_{ind}\tilde{\boldsymbol{\Phi}}(t_k) + \boldsymbol{\Psi}(t_k), \delta_s\right) \leq \boldsymbol{0} \qquad & k = 1, \ldots, p.
\end{aligned} \tag{26}$$

With high confidence $1 - \beta$, the solution of 26, is feasible in a subset $\Delta_\epsilon \subset \Delta$ such that the probability of Δ_ϵ is no smaller than $1 - \epsilon$.

2. Application to the differential drag rendez-vous

The dynamical model used by the planner are the linearized in-plane Schweighart-Sedwick equations[12] applied to the curvilinear relative states:

$$\frac{\mathrm{d}\tilde{\boldsymbol{w}}}{\mathrm{d}t} = \begin{bmatrix} 0 & 0 & 1 & 0 \\ 0 & 0 & 0 & 1 \\ \left(5c^2-2\right)\omega_{orb}^2 & 0 & 0 & 2\omega_{orb}c \\ 0 & 0 & -2\omega_{orb}c & 0 \end{bmatrix} \tilde{\boldsymbol{w}} + \begin{bmatrix} 0 \\ 0 \\ 0 \\ 1 \end{bmatrix} \Delta f_d\left(t, \boldsymbol{w}, \delta, u\right), \tag{27}$$

where ω_{orb} and c are the constant angular orbital velocity and the Scweighart-Sedwick coefficient defined in Section 4.A, respectively. These equations assume a circular reference orbit, secular-only perturbations of the Earth oblateness, J_2.

According to the assumptions introduced in Section 4.A, we note that the differential drag is linear in u, i.e., it can be recast in the form:

$$\Delta f_d\left(t, \boldsymbol{w}, \delta, u\right) = \Delta f_{d,u}\left(t, \boldsymbol{w}, \delta\right) u + \Delta f_{d,0}\left(t, \boldsymbol{w}, \delta\right) \tag{28}$$

The system 27 is differentially flat. It can be verified that a possible flat output for the system is

$$q = \mathcal{Q}\left(\tilde{\boldsymbol{w}}, u, \dot{u}, ...\right) = \frac{\dot{\tilde{x}} - 2\omega_{orb}c\ \tilde{y}}{\left(5c^2-2\right)\omega_{orb}^2} \tag{29}$$

and the corresponding mapping of the states and control are

$$\begin{aligned} \tilde{\boldsymbol{w}} &= \boldsymbol{\mathcal{W}}\left(q, \dot{q}, ...\right) = \begin{bmatrix} \dot{q} \\ \frac{\ddot{q} - \left(5c^2-2\right)\omega_{orb}^2 q}{2\omega_{orb}c} \\ \ddot{q} \\ \frac{q^{(3)} - \left(5c^2-2\right)\omega_{orb}^2 \dot{q}}{2\omega_{orb}c} \end{bmatrix} \\ u &= \mathcal{U}\left(q, \dot{q}, ...\right) = \frac{\frac{q^{(4)} - \left(c^2-2\right)\omega_{orb}^2 \ddot{q}}{2\omega_{orb}c} - \Delta f_{d,0}\left(t, \boldsymbol{\mathcal{W}}\left(q, \dot{q}, ...\right), \delta\right)}{\Delta f_{d,u}\left(t, \boldsymbol{\mathcal{W}}\left(q, \dot{q}, ...\right), \delta\right)} \end{aligned} \tag{30}$$

The constraints impose that the control variable, u, is bounded between -1 and 1. It follows

$$\begin{aligned} \frac{q^{(4)}(t_k) - \left(c^2-2\right)\omega_o r b^2 \ddot{q}(t_k)}{2\omega_{orb}c} &\leq \Delta f_{d,u}\left(t, q, \dot{q}, ..., \delta\right) + \Delta f_{d,0}\left(t, q, \dot{q}, ..., \delta\right) \\ \frac{q^{(4)}(t_k) - \left(c^2-2\right)\omega_o r b^2 \ddot{q}(t_k)}{2\omega_{orb}c} &\geq -\Delta f_{d,u}\left(t, q, \dot{q}, ..., \delta\right) + \Delta f_{d,0}\left(t, q, \dot{q}, ..., \delta\right) \end{aligned} \qquad k = 1, \ldots, p. \tag{31}$$

We note that the constraints in Equation (31) are not convex in $(q, \dot{q}, \ldots)$. This is due to the fact that the simple density model depends on the relative position. However, for relatively small distances (say few hundred kilometers in-track and and few hundred meters radial), it can be safely assumed that the local density is the same for the two satellites. In this way, the right hand term of the equations becomes independent on the flat outputs, and the set of constraints is convex. This assumption was made in the simulations presented in Section V. Alternatively, a conservative approach consists in building a convex inner polytope approximation of the constraints as proposed in.[16]

4.C. On-line compensator

On-line compensation is mandatory to account for non-modeled dynamics in the control plant and uncertainties, whose effect is the deviation of the real trajectory from the scheduled one.

A model predictive control (MPC) algorithm is exploited for this purpose. At each evaluation, the on-line compensator solves a problem analogous to the maneuver planner. The only differences are the boundary conditions, the fixed horizon, and the performance index.

Initial conditions are provided by the current states at the beginning of the evaluation at time t. MPC is based upon the receding horizon principle, so that the final time is not dependent on event constraints like

in Equation (19), but the horizon is fixed to $t + t_h$. The computed corrected control is then applied to the plant for a time $t_c \leq t_h$.

The cost function is aimed at minimizing the divergence from the reference path:

$$\mathcal{J}_{on-line} = \int_t^{t+t_h} \left(\boldsymbol{q}(t) - \boldsymbol{q}^*(t)\right)^T \mathrm{P} \left(\boldsymbol{q}(t) - \boldsymbol{q}^*(t)\right) \, \mathrm{d}t \tag{32}$$

where P is a positive definite matrix of user-supplied weights, $\boldsymbol{q} = \left[q, \dot{q}, \ddot{q}, q^{(3)}\right]^T$, and the symbol * indicates the reference path obtained from the solution of Problem (26).

V. Numerical simulations

The proposed case study consists of the rendez-vous between two satellites of the QB50 constellation.[17] QB50 will be a constellation of 40 Double and 10 triple CubeSats.[18] The launch is planned for 2016. The constellation will be deployed on a highly-inclined near-circular LEO and the satellites will be separated by several tens or hundreds kilometers.

The QB50 requirements for the 'standard 2U CubeSats'[19] impose that the long axis of the CubeSat must be aligned with the orbital velocity. One of these standard CubeSats is considered to be the target. QARMAN, a 3U CubeSat of the constellation developed by the Von Karman Institute for Fluid dynamics and the University of Liège, will be the chaser. Both the target and the chaser are assumed to be provided with 3-axis magnetotorquers and 3 reaction wheels with spin axes aligned with the edges of the CubeSat. Quaternion feedback algorithm is exploited to follow the required attitude of the two satellites.

The target is assumed to be passive, i.e., its ballistic coefficient cannot be controlled. The target's reference attitude is 3-axis stabilized in its minimum-drag configuration, i.e., with its long axis aligned toward its orbital velocity direction, $\boldsymbol{v}_t$. Differential drag is imposed by changing the ballistic coefficient of the chaser. This is achieved by pitching the chaser about the orbital normal direction, $\hat{\boldsymbol{z}}$.

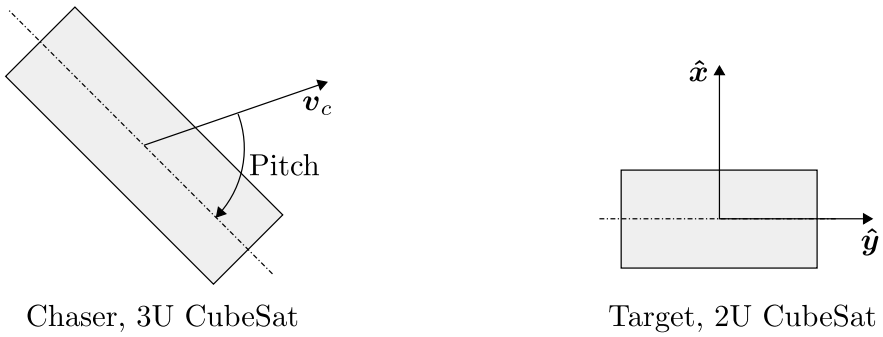

Figure 3. Attitude dynamics notation. The target is supposed to fly with the long axis aligned to the orbital velocity direction.

Table 1 lists the input parameters of the numerical simulations.

5.A. Simulation environment

The numerical simulations performed in this study are carried out in a highly detailed environment. Both attitude and orbital dynamics are propagated in their complete non-linear coupled dynamics.

The orbital perturbations include aerodynamic force, a detailed gravitational field with harmonics up to order and degree 10, solar radiation pressure and third-body perturbations of sun and moon. The external torques are due to aerodynamics and gravity gradient, and the models proposed by Wertz[20] for the reaction wheels and magnetic rods are exploited.

In this study, the modeling of the aerodynamic perturbation assumes thermal flow, variable accommodation of the energy, and non-zero re-emission velocity. Under these hypotheses, the three extensively-used simplifications involved in drag modeling fall into defect. Specifically, it is not true that the drag is the only component of the aerodynamic force, that the drag coefficient is constant, and that the drag is proportional to the surface exposed to the incoming flow. For complex satellite geometries, direct simulation

Table 1. Simulation parameters.

	Julian date	01/04/2016 00:00 UTC
	Maneuvering time	150 hhours
Mean elements of the target	semi-major axis	$6758 \cdot 10^3$ m
	eccentricity	0.001
	inclination	98 deg
	RAAN	45 deg
	argument of perigee	0 deg
	true anomaly	0 deg
Initial relative states	in-track position , i.e., $\tilde{y}$	$50 \cdot 10^3$ m
	radial position, i.e., $\tilde{x}$	100 m
	in-track velocity, i.e., $\tilde{v}_y$	0 m s^{-1}
	radial velocity, i.e., $\tilde{x}$	0 m s^{-1}
	differential orbital inclination	0.01 deg
	differential RAAN	0.01 deg
Space weather at $t = 0s$	Daily solar flux	150 sfu
	81-day averaged flux	130 sfu
	geomagnetic index A_p	27
Target properties	mass	2 kg
	dimensions	$0.1 \times 0.2 \times 0.1$ m^3
	inertia	$I_y = 8 \cdot 10^{-3}$ kg m^2, $I_x = I_z = 3 \cdot 10^{-3}$ kg m^2
Chaser properties	mass	4 kg
	dimensions	$0.1 \times 0.3 \times 0.1$ m^3
	inertia	$I_y = 25 \cdot 10^{-3}$ kg m^2, $I_x = I_z = 5 \cdot 10^{-3}$ kg m^2
Attitude actuators	wheels' maximum torque	$0.03 \cdot 10^{-3}$ N m
	wheels' operating range	$[-6000, 6000]$rpm
	wheels' inertia	$0.25 \cdot 10^{-6}$ kg m^2
	Magnetic rods' dipole	0.2 A m^2

Monte Carlo is arguably the only way of computing these coefficients. However, this technique is extremely computationally intensive. For simple convex geometries, semi-empirical analytic methods relying on the decomposition into elementary panels provide an accurate and computationally-effective alternative. The semi-analytic method considered in this work is based upon the research of Sentman[21] and Cook[22] and upon the more recent contributions summarized in.[23]

This model was used in our orbital propagator to compute the aerodynamic coefficients of the satellites at every time step. The two satellites are modeled with a parallelepiped shape and the principal axes are assumed to be aligned with the edges of the parallelepiped. This is very appropriate when considering satellites with body-mounted solar arrays. The contribution to the aerodynamic force and torque of possible appendices, e.g., antennas, is neglected.

The atmospheric model exploited in the propagator is NRLMSISE-00. Short-term random variations are included by adding a second-order stationary stochastic process to the total mass density. The power spectral density of the process is the one proposed by Zijlstra[24] rescaled for the altitude of the maneuver. The atmosphere is assumed to co-rotate with the Earth, but thermospheric winds are neglected.

The realization of the trajectories of the space weather proxies is performed by exploiting the same Gaussian cupola presented in Section 4.A.

Table 2 summarizes the main features of the simulation environment and it compares them to the counterpart of the control plant discussed in Section 4.B.

5.B. Results

The main purpose of these simulations is to assess the benefit of using the robust reference trajectory against a non-robust one. For this reason, a Monte Carlo analysis is carried out as follows:

- a single propagation is performed from $t = 0$ to $t = t_{obs}$. The deterministic and probabilistic model of the drag are estimated;
- a *nominal* and a *robust* and reference trajectory are generated. The nominal one is generated without the scenario approach by using the only deterministic contributions to the drag, i.e., estimated ballistic

Table 2. Differences between the simulation environment and the plant of the controller.

	Simulation environment	**Control plant**
Orbital dynamics	Full non-linear osculating relative dynamics.	Linearized equations for mean curvilinear relative states.
Attitude dynamics	3 DoF Euler equations.	None.
Atmospheric model	NRLMSISE-00 with short-term stochastic variations. Geodetic altitude from the reference ellipsoid. Space weather proxies modeled with set of correlated random variables.	Exponential vertical structure and sinusoidal periodic variations (day-night). Geocentric altitude from the reference ellipsoid.
Aerodynamic force	Sentman's model with more recent updates.	Drag force only. Linear relationship between ballistic coefficient and exposed cross section. Probabilistic model for random variations.
Gravitational model	Harmonics up to order and degree 10.	J_2 secular effect.
Other perturbations	Luni-solar third-body perturbations, solar radiation pressure.	None.
External torques	Gravity gradient and aerodynamic torque computed on with the Sentman's model and more recent updates.	None.
Attitude control	Three-axis magnetic coils and three reaction wheels. Quaternion feedback control algorithm. Mangetic coils desaturate wheels in permanence.	None.

coefficients, the simple atmospheric model $\rho(r, \theta, i; A, B, C, D)$, and seasonal component of the SARMA process characterizing γ_{fast}. The robust trajectory is computed by setting the risk and confidence parameters of the scenario approach to $\epsilon = 0.1$, and $\beta = 10^{-3}$, respectively;

- starting from $t = t_{obs}$, 1000 realizations of the stochastic processes related to the space weather proxies are generated by exploiting the conditional probability of the Gaussian cupola defined in Equation (17) given the values of the proxies for $t < t_{obs}$. The on-line propagation is performed for each realization;

The results obtained for the three modules of the controller are analyzed in the following.

1. Probabilistic drag estimator

In this work, we selected an observation time equal to $t_{obs} = 8t_{orb}$.

Figure 4(a) compares the real drag force of the target with the one estimated with the deterministic component of the drag estimator. The drag estimated with the Jacchia 71 model, which was used to tune the simplified model, is also illustrated. As anticipated in Section 4.A, the controller ignores the exact structure of the atmosphere. This is emphasized by the relevant difference between the estimated and the real drag force in Figure 4(a). Nonetheless, the good match between the simple and the largely more advanced Jacchia 71 model, validates our claim stating that the former is able to detect the main features of the structure of the upper atmosphere.

The *fast* variations model, $\gamma_{fast}(t, \delta)$ and the estimation dataset introduced in Equation (16) are illustrated in Figure 4(b). The seasonal component corresponding to the orbital period is well defined, and it can be checked that its peaks roughly correspond to the peaks of maximum discrepancy between the real and the estimated drag in Figure 4(a).

Concerning the *slow* variations model, Figures 5(a) and 5(b) illustrates the identified probability distribution of the space weather proxies on a period of $t_{proc} = 20$ days. The autocorrelation of the daily solar flux smoothly decreases with the time increment, while the one of the 81-day averaged flux is always close to one. This is due to the fact that the averaged flux exhibits negligible variations within the window $[0, t_{proc}]$. Nonetheless, if the initial value of the proxies is changed, large variations can be expected from one realization of the process to the other according to the marginal distribution. Indeed, high values of the daily flux are expected when its average is also high. This consideration is consistent with the high cross correlation between daily and averaged values. These considerations are supported by Figure 5(c), which shows few trajectories generated with the identified distribution and the initial conditions listed in Table 1. The low values of both the autocorrelation of $\mathbf{A}_p$ and its correlation with the other variables emphasize

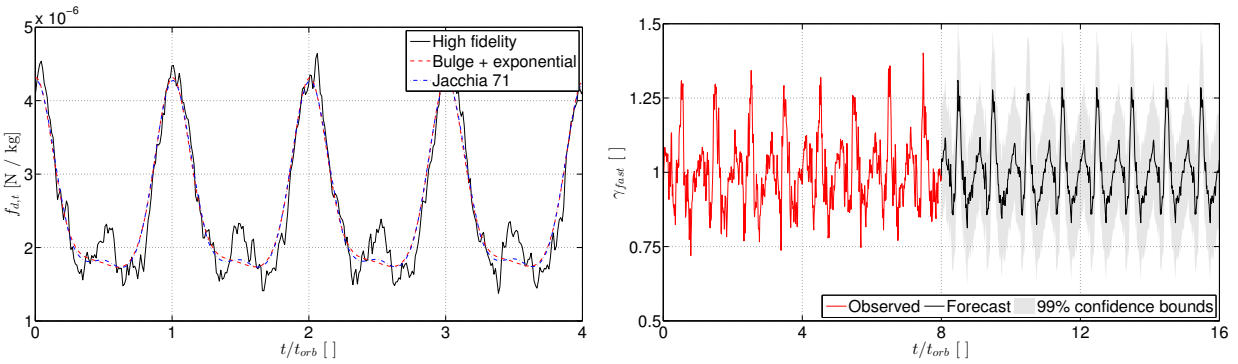

(a) Real and simulated drag on the target. The red dashed line is the deterministic component provided by the drag estimator.

(b) Short terms drag variations. Data used to fit the SARMA model are in red. Forecast of the SARMA model and 99% confidence bounds are in black and grey, respectively.

Figure 4. Deterministic drag model and *fast* stochastic variations.

that the geomagnetic activity is a largely more rapid process with respect to the others and, as such, more difficult to predict.

2. *Maneuver planner*

The selected objective function is aimed at minimizing the amplitude of the oscillations in the $\tilde{x}-\tilde{y}$ diagram. It can be proven that this conditions is satisfied by $\mathcal{J} = \int_0^{t_f} \tilde{v}_x^2 \mathrm{d}t$.

In this paper, because of their simple implementation, truncated Fourier series with fundamental frequency $f = \frac{1}{2t_f}$ are used for the basis of the flat outputs, i.e.,

$$\mathbf{\Phi}^{(i)}(t) = \begin{bmatrix} 0^i \\ (2\pi f)^i \cos\left(2\pi f t + 0.5\pi i\right) \\ (2\pi f)^i \sin\left(2\pi f t + 0.5\pi i\right) \\ (4\pi f)^i \cos\left(4\pi f t + 0.5\pi i\right) \\ (4\pi f)^i \sin\left(4\pi f t + 0.5\pi i\right) \\ \vdots \end{bmatrix}. \tag{33}$$

The series is truncated when harmonics become smaller than half of the orbital period. A uniform temporal grid of check points with frequency resolution 10 times larger than the highest frequency of the expansion is considered. This is estimated large enough to prevent relevant violation between check points.

The blue curve in Figure 6 illustrates the bounds imposed to the differential drag by the deterministic components of the estimated drag. The light-red region is the envelop of the samples required by the scenario approach generated with the stochastic model. The bounds in the robust case (red curves) are given by the worst case of all these samples and, indeed, they are narrower with respect to the ones of the nominal case. These bounds become closer and closer as time passes. This is due to the fact that *slow* variations due to $\gamma_{slow}(t,\delta)$ might yield to much lower levels of the atmospheric density at the end of the maneuver compared to the initial one (which is used to fit the deterministic component of the drag model). In addition, the robust bounds are also narrower than the nominal ones at the very beginning because of the *fast* variations.

The robust and nominal reference path are illustrated in Figure 7(a). As expected, the nominal solution is 'smoother', i.e., it is more optimal than the robust one. This is due to the fact that the available differential drag is larger than in the case of the robust solution, as illustrated in Figure 7(b). Nonetheless, the solution obtained in the nominal case is evidently infeasible for the bounds imposed in the robust case.

3. *On-line compensator*

Figure 8 illustrates the tracking error of the relative states for the 1000 Monte Carlo samples. The robust solution performs better than the nominal one for all the components, in particular in the final part of

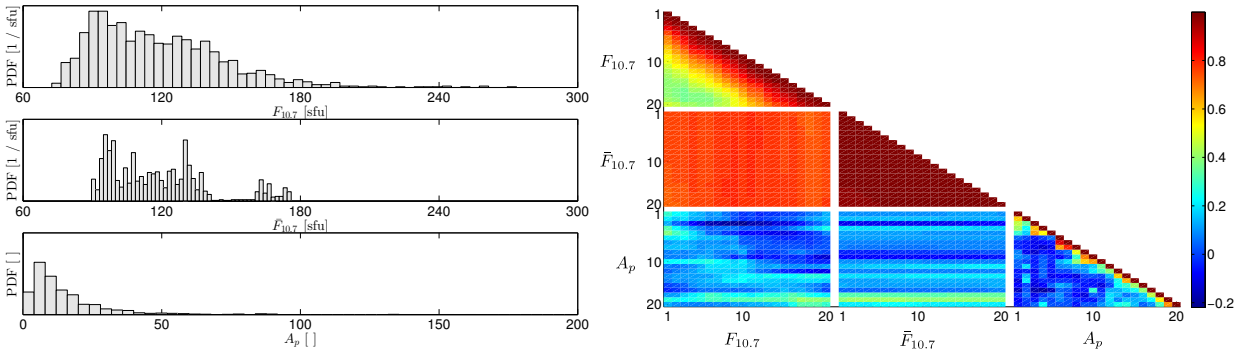

(a) Marginal distributions

(b) Correlation matrix

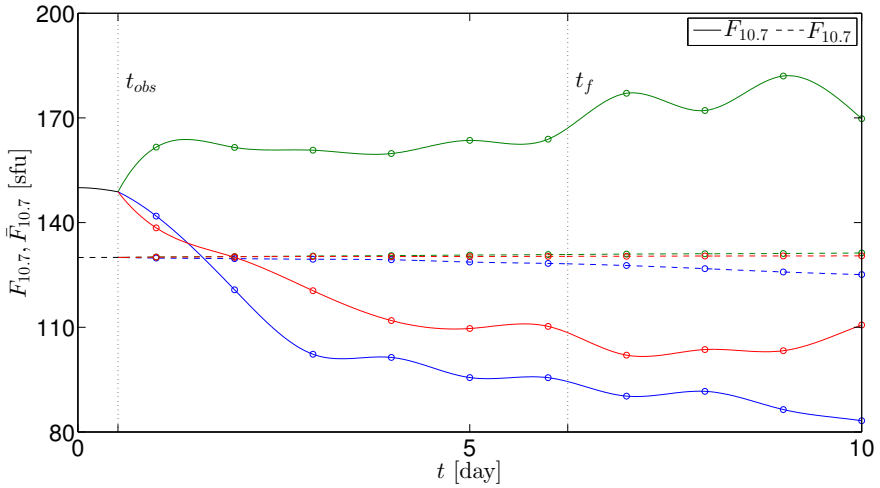

(c) Three realizations of stochastic trajectories of $F_{10.7}$ and $\bar{F}_{10.7}$. The circles are the points corresponding to the elements of the vectors $\mathbf{F}_{10.7}$ and $\bar{\mathbf{F}}_{10.7}$.

Figure 5. Probabilistic model for the space weather proxies $F_{10.7}$, $\bar{F}_{10.7}$, A_p.

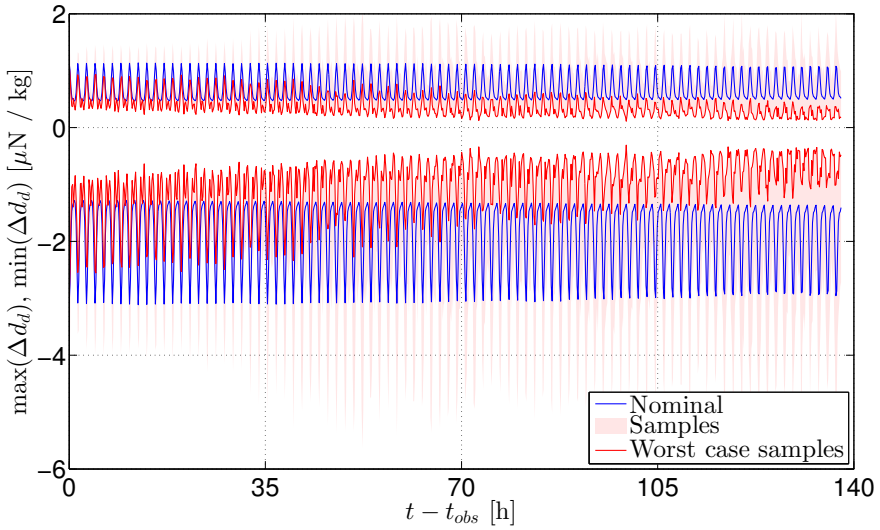

Figure 6. Differential drag bounds. The colored region is the envelop of the samples required by the scenario approach. Solid red lines are the worst case of these samples.

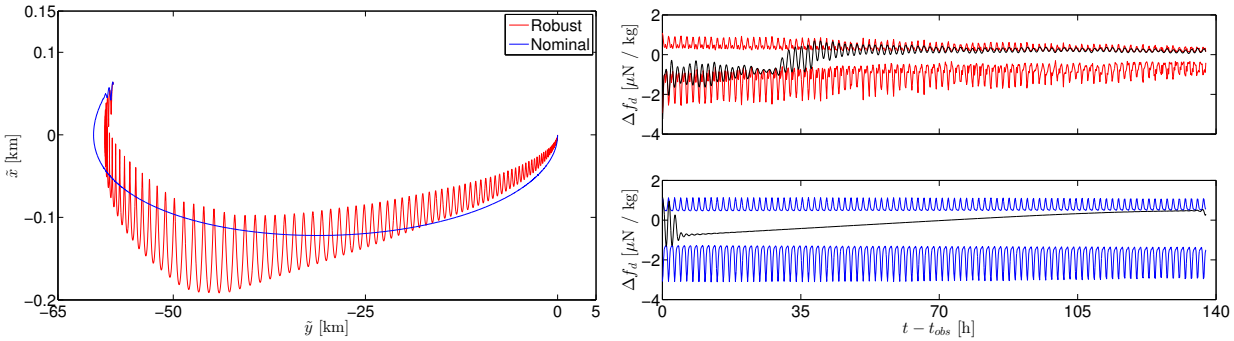

(a) Trajectory.

(b) Differential drag.

Figure 7. Scheduled reference path. The nominal solution is more optimal than the robust one in the sense that it achieves a 'smoother' path. However, the nominal solution is infeasible for the bounds imposed in the robust counterpart.

the maneuver, where the robust solution is much more conservative than the nominal one because of the long-term drift. This results in an enhancement of the satisfaction of the rendez-vous conditions.

The probability distribution of the root mean square tracking error for the two reference paths is illustrated in Figure 9. Also in this case, the tracking of the robust reference path is systematically better than the nominal one. In addition, not only the peaks of the distributions in the robust case are shifted to the left, but also they are higher, i.e., narrower distribution. Finally, the better performance of the tracking in the robust case can also be appreciated in Figure 10, where 99% percentiles of the on-line trajectories are superimposed to the reference path. At the end of the maneuver, these bounds are much closer to the origin when using the robust reference trajectory.

VI. Conclusions

A robust control algorithm for the differential-drag based rendez-vous was proposed. The core of the algorithm is the computation of a robust reference trajectory which is feasible for the largest majority of the uncertainties. The method relies on a probabilistic estimation of the aerodynamic drag based on observations of the spacecraft position and historical data of the space weather proxies.

The developments were validated by means of high fidelity simulations and showed that using a robust reference path is beneficial in terms of the tracking accuracy of the reference path itself.

Acknowledgments

The author Lamberto Dell'Elce would like to acknowledge the Belgian National Fund for Scientific Research for its financial support (FRIA fellowship).

References

[1]Leonard, C.L., "Formation keeping of spacecraft via differential drag," M.Sc. Thesis, Massachusetts Institute of Technology, Cambridge, 1986.

[2]Bevilacqua, R., and Romano, M., "Rendezvous maneuvers of multiple spacecraft using differential drag under J_2 perturbation," Journal of Guidance, Control, and Dynamics, vol. 31, 2008, 1595-1607.

[3]Ben-Yaacov, O., and Gurfil, P., "Long-Term Cluster Flight of Multiple Satellites Using Differential Drag," Journal of Guidance, Control, and Dynamics, vol. 36, No. 6, 2013, 1731-1740.

[4]Dell'Elce, L., and Kerschen, G., "Comparison between analytical and optimal control techniques in the differential drag based rendez-vous," 5th International Conference on Spacecraft Formation Flying Missions and Technologies, Munich, Germany, 2013.

[5]Dell'Elce, L., and Kerschen, G., "Robust rendez-vous planning using the scenario approach and differential flatness," 2nd IAA Conference on Dynamics and Control of Space Systems, Rome, Italy, 2014.

[6]Calafiore, G., and M. C. Campi, M.C., "Uncertain convex programs: Randomized solutions and confidence levels," Mathematical Programming, 102, 2005, pp. 25–46.

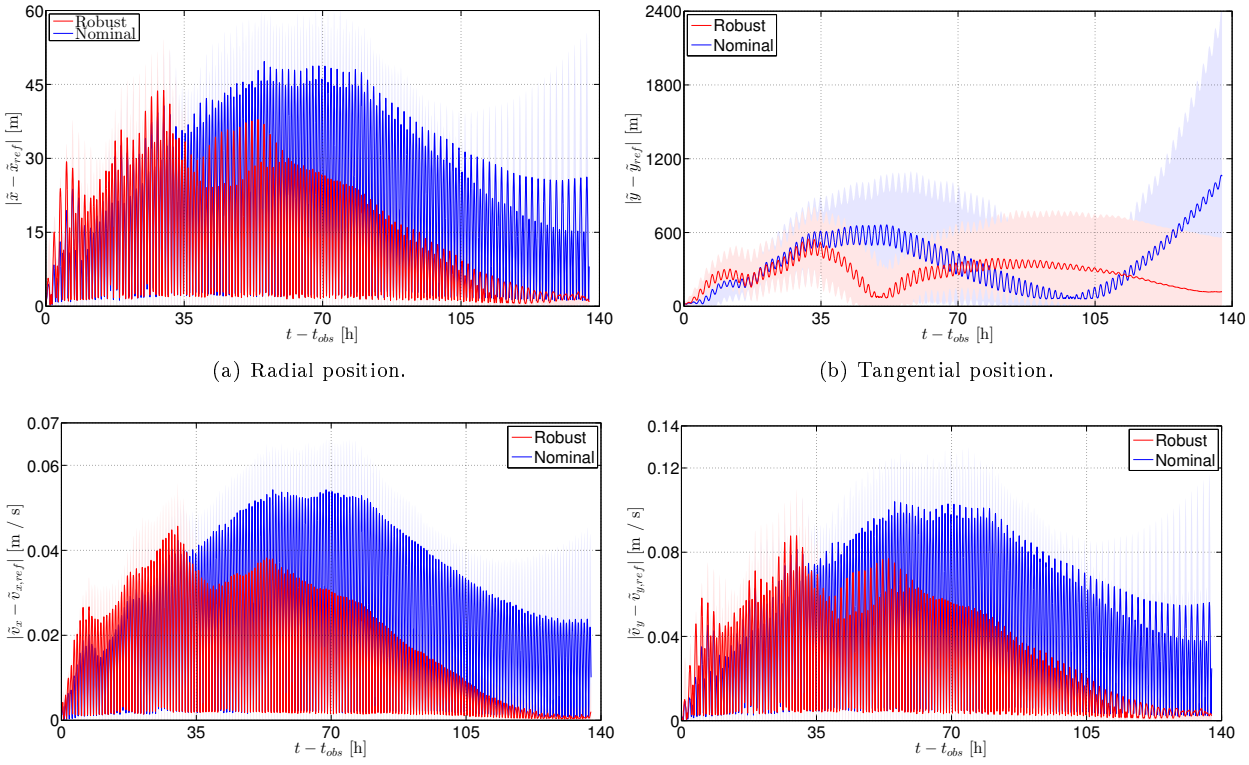

(a) Radial position.

(b) Tangential position.

(c) Radial velocity.

(d) Tangential velocity.

Figure 8. Tracking error for the 1000 Monte Carlo simulations. Solid curves are the median of the 1000 Monte Carlo samples, while coloured bounds are 99% confidence bounds. Red and blue are related to the tracking of the robust and of the nominal reference path, respectively.

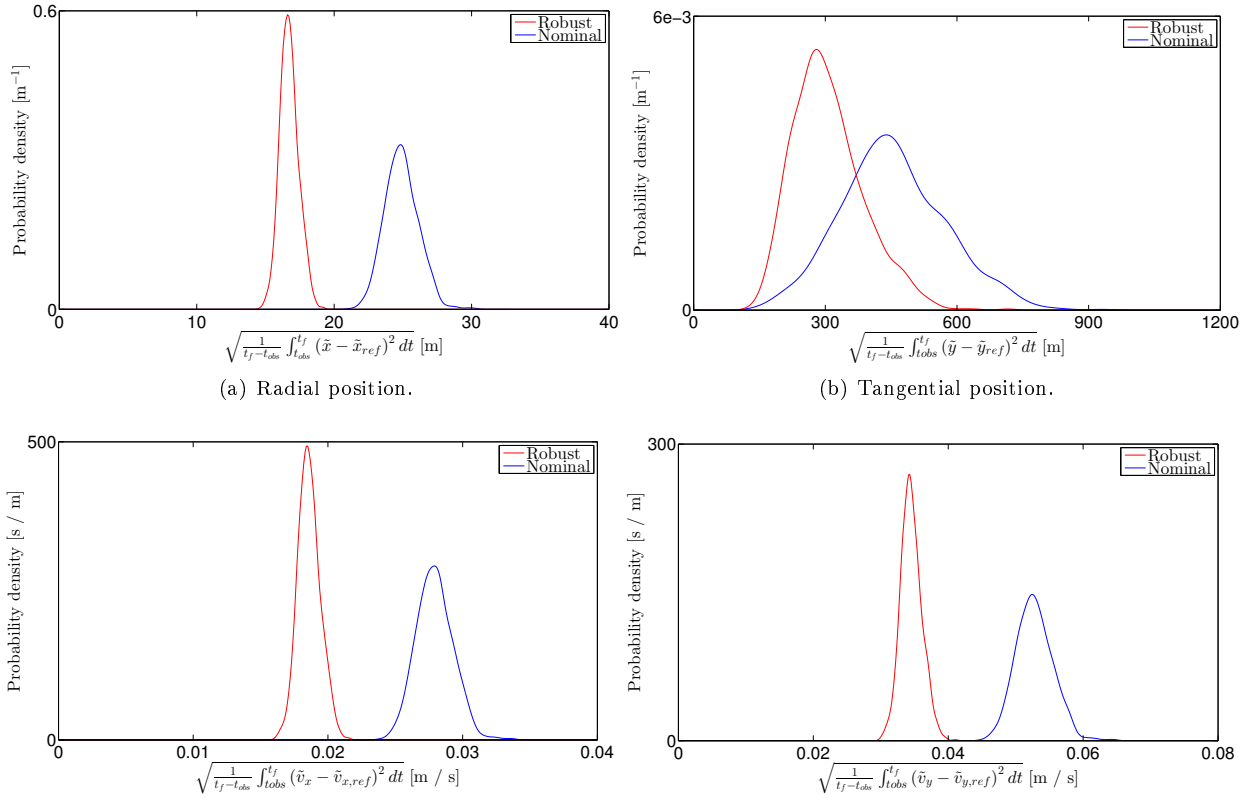

(a) Radial position.

(b) Tangential position.

(c) Radial velocity.

(d) Tangential velocity.

Figure 9. Probability density distribution for the root mean square error between planned and on-line trajectory. Red and blue are related to the tracking of the robust and of the nominal reference path, respectively.

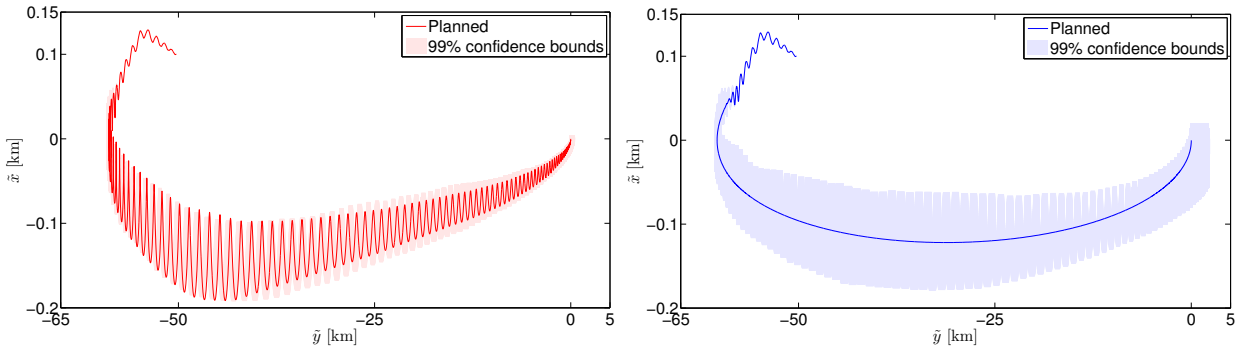

(a) Robust reference path.

(b) Nominal reference path.

Figure 10. Comparison between the reference trajectories and the Monte Carlo samples. The colored regions indicate 99% confidence bounds on the trajectory of the samples. The tracking of the reference path is better with the robust reference path.

[7]Calafiore, G., and Campi, M.C., "The scenario approach to robust control design," IEEE Transactions on Automatic Control, 51, 2006, pp. 742–753.

[8]Campi, M.C., and Garatti, S., "The exact feasibility of randomized solutions of robust convex programs," SIAM Journal on Control and Optimization, 19(3), 2008, pp. 1211–1230.

[9]Fliess, M., Lévine, J., Martin, P., and Rouchon, P., "Flatness and defect of non-linear systems: introductory theory and examples," International Journal of Control, 61(6), 1995, pp. 1327–1361.

[10]Louembet, C., "Collision avoidance in low thrust rendezvous guidance using flatness and positive B-splines," proceedings of the American Control Conference 2011 (ACC 2011).

[11]Ben-Yaacov, O., Gurfil, P., "Orbital Elements Feedback for Cluster Keeping Using Differential Drag," 2nd IAA Conference on Dynamics and Control of space Systems, Rome, Italy.

[12]Schweighart, S.A., Sedwick, R.J., "High-fidelity linearized J2 model for satellite formation flight," Journal of Guidance, Control, and Dynamics, Vol. 25, 1073–1080, 2002.

[13]Dell'Elce, L., Arnst, M., and Kerschen, G., "Probabilistic assessment of the lifetime of low-Earth-orbit spacecraft: uncertainty characterization," Journal of Guidance, Control, and Dynamics, 2014. DOI: 10.2514/1.G000148

[14]Dell'Elce, L., Kerschen, G., "Validation of differential drag propellantless maneuvers using 6 DoF simulations and stochastic dynamics," 9th ESA International Conference on Guidance, Control, and Dynamics, Porto, Portugal, 2014.

[15]CelesTrak Database, URL `http://www.celestrak.com/SpaceData/sw19571001.txt`.

[16]Faiz, N., Agrawal, S.K., and Murray, R.M., "Differentially flat systems with inequality constraints: an approach to real-time feasible trajectory generation," Journal of Guidance, Control and Dynamics, 2001.

[17]Muylaert, J., *et al.*, "QB50: An International Network of 50 Cubesats for Multi-Point, In-Situ Measurements in the Lower Thermosphere and for Re-Entry Research", ESA Atmospheric Science Conference, Barcelona, Spain, 2009.

[18]Heidt, H., Puig-Suari, J., Moore, A., Nakasuka, S., and Twiggs, R., "CubeSat: A new generation of picosatellite for education and industry low-cost space experimentation" Small Satellite Conference, Logan, US, 2000.

[19]Muylaert, J., "Call for CubeSat Proposals for QB50", Von Karman Institute for Fluid Dynamics, 2012.

[20]Wertz, J.R., "Spacecraft attitude determination and control," Kluwer academic publishers, Dordrecht, The Netherlands, 1978.

[21]Sentman, L.H., "Free Molecule Flow Theory and its Application to the Determination of Aerodynamic Forces", Technical Report LMSC-448514, Lockheed Missiles & Space Company, 1961.

[22]Cook, G.E., "Satellite Drag Coefficients", Planetary and Space Science 13, 929–946, 1965.

[23]Doornbos, E., "Thermospheric Density and Wind Determination from Satellite Dynamics," Springer, Series: Springer Theses, 2012.

[24]Zijlstra, M., Theil, S., "Model for Short-term Atmospheric Density Variations," Earth Observation with CHAMP, Springer Berlin Heidelberg, 2005.